

www.acsami.org Research Article

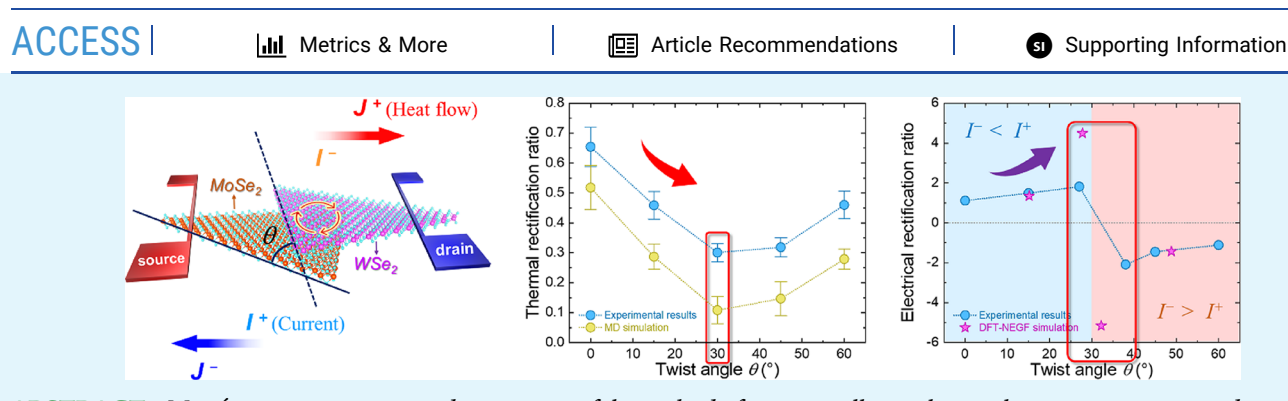
Moiré-Engineering-Induced Counteractive Control of Thermal and Electrical Transport in MoSe₂/WSe₂ Heterostructure

Haidong Wang,*,# Yaohong Zhou,# Siqi Xie,# Jie Zheng, Hongxin Zhu, and Bingyang Cao*



Cite This: ACS Appl. Mater. Interfaces 2025, 17, 57403-57413

Read Online



ABSTRACT: Moiré engineering provides a powerful method for controlling electrical transport in two-dimensional semiconductors. Meanwhile, moiré engineering also enables the tuning of the interfacial thermal conductance of bilayer materials by means of changing the distance between layers. However, the simultaneous control of electrical and thermal transport in the same moiré-engineered bilayer sample can be challenging. The mechanism underlying the differentiated regulation effect remains elusive. In this work, the electrical and thermal conductivities of the same MoSe₂/WSe₂ heterostructure were measured simultaneously with a series of precisely controlled twist angles. It is found that as the moiré superlattice period declines with the twist angle increasing from 0° to 30°, the thermal rectification ratio of the heterostructure decreases from 65 to 30%, meanwhile the electrical rectification ratio increases from 100 to 200%. At a critical twist angle of 30° corresponding to the minimum moiré superlattice period, the thermal rectification ratio is minimized, while the electrical rectification undergoes a reversal from a positive to a negative state. This demonstrates that the moiré superlattice provokes different rectifying responses for phonons and electrons. Decreasing the period of the moiré superlattice induces a pronounced enhancement of the asymmetry in the electronic density of states, while the thermal asymmetry is suppressed due to stronger interlayer coupling. These findings furnish fresh perspectives on the moiré-controlled effect and establish a basis for the development of advanced atomic-scale rectifying devices.

KEYWORDS: van der Waals heterostructure, moiré superlattice, twist angle control, electron and phonon transport, rectification

■ INTRODUCTION

Leveraging the outstanding physical properties inherent in two-dimensional (2D) materials, $^{1-10}$ the van der Waals heterostructure, constructed through the stacking of 2D materials, 11-23 manifests even more novel and remarkable properties upon the introduction of twisting as an additional modulation parameter.^{24–26} When two layers of structurally identical or similar materials are stacked under a slight misalignment, periodic interference moiré patterns emerge on the surface, differing from the original lattice. The morphology of the moiré superlattice can be precisely regulated by modulating the degree of misalignment. Specifically, this can be achieved by finely tuning the relative twist angle between bilayers. Most research efforts have been focused on electrical properties, generating the field of "Twistronics". 27 For instance, twisted bilayer graphene at a magic angle of 1.1° forms flat bands that induce unconventional superconductivity²⁸ and correlated insulating states²⁹ owing to the electron-electron interactions modulated by

moiré superlattice. In transition metal dichalcogenide (TMD) bilayers such as MoS_2/WSe_2 , twist-induced flat bands can be described using exotic electronic models, including strongly asymmetric p_x-p_y Hubbard models, 30 and enable the control of exciton properties, such as those of long-lived indirect excitons, 31 for applications in valleytronics. 32 Twisted bilayer h-BN forms triangular lattices 33 at small twist angles, enabling topological phases including quantum spin liquids and topological superconductivity. 34

Recently, it has been confirmed by simulations^{35–45} and experiments^{46–48} that the twist-controlled moiré superlattice exerts similar regulatory effect on the phonon transport as on

Received: June 17, 2025 Revised: September 24, 2025 Accepted: September 26, 2025 Published: October 4, 2025





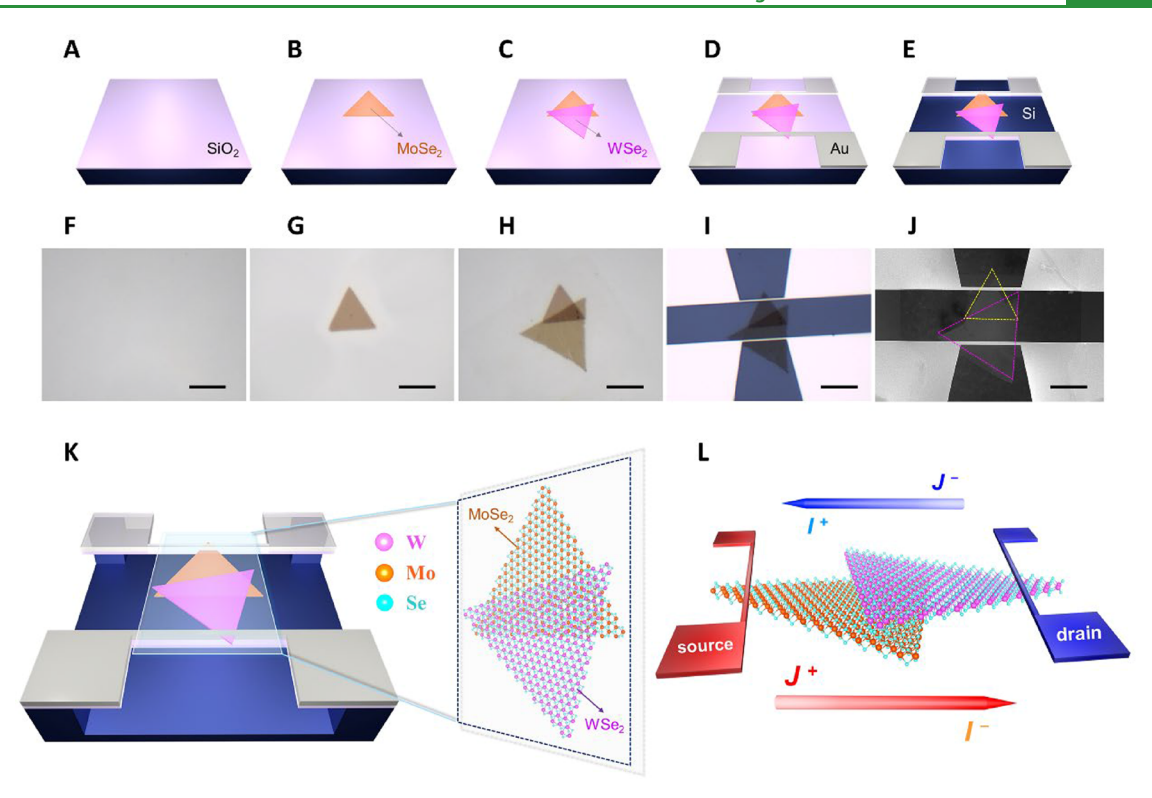


Figure 1. Fabrication process of the suspended H-type devices containing the stepwise stacked MoSe₂/WSe₂ van der Waals heterostructures and the schematic diagram of measurements. (A) Clean SiO₂/Si substrate. (B) Transfer of single-crystalline MoSe₂ monolayer. (C) Transfer of singlecrystalline WSe₂ monolayer. (D) Deposition of H-type Au nanosensors and electrodes. (E) Reactive etching of SiO₂ layer and XeF₂ etching of Si substrate to fully suspend the H-type sensing device. (F-J) Optical and SEM images of the stepwise stacked heterostructure sample at each step with 10 µm scale bar (video is available in the SI). (K) Structure of MoSe₂/WSe₂ van der Waals heterostructure with a controlled twisting angle in between. (L) Schematic diagram showing the bidirectional thermal and electrical measurements.

the electron transport. In twisted bilayer and multilayer van der Waals heterostructures, both in-plane and out-of-plane thermal conductivities exhibit a prominent correlation with the twist angle. A striking example is found in twisted bilayer graphene, where the thermal conductivity reaches a local minimum as the twist angle approaches the so-called "thermal magic angle", mirroring the behavior observed in the electronic systems.³ Although Jiang et al. have established an analytical relation between the interfacial thermal conductivity and the twist angle in twisted 2H-TMD stacks, 42 the field remains predominantly theoretical and simulation-based. Precise experimental characterization of thermal transport in twisted structures continues to pose a significant challenge. Moreover, while prior studies have independently controlled the thermal or electrical transport in twisted bilayers, the simultaneous manipulation of both transport channels within the same device remains largely unexplored and experimentally unvalidated. The mechanisms ^{49,50} by which moiré superlattices influence phonon and electron transport, particularly the regulation of phonon pathways, scattering, and coupling with electronic states owing to the interlayer interactions, remain unclear.51,52

In this work, we have specially designed and fabricated a stepwise stacked MoSe₂/WSe₂ heterobilayer device, where the single-crystalline MoSe₂ and WSe₂ monolayers partially overlap in the center. By precisely controlling the twist angle at the interface of the heterobilayer, the pattern of moiré superlattice can be tuned continuously. The heterobilayer device is precisely suspended between two individual Au (gold) nanosensors. Electrons and phonons excited at one sensor

are compelled to traverse the overlapping heterointerface to reach the other sensor. This setup enables a substantial enhancement of the modulation effect within the moiré superlattice. An inverse rectifying effect of the moiré superlattice on the electron and phonon transport has been observed in the experiment. The thermal rectification ratio decreases from 65 to 30% as the moiré superlattice period declines with the twist angle increasing from 0° to 30°; meanwhile, the electrical rectification ratio increases from 100 to 200%. At a critical twist angle of 30° corresponding to the minimum moiré superlattice period, the thermal rectification ratio is minimized, while the electrical rectification undergoes a fierce change from positive to negative. The result demonstrates that the moiré-controlled heterointerface provokes different responses for phonons and electrons. The asymmetry in phonon transport is weakened as the moiré superlattice period declines, but the asymmetry in electron transport is strengthened in contrast. A quantitative explanation is provided through detailed nonequilibrium molecular dynamics simulations and density functional theory calculations.

■ RESULTS AND DISCUSSION

Fabrication of the Stepwise Stacked MoSe₂/WSe₂ van der Waals Heterostructures. Triangular MoSe₂ and WSe₂ single-crystalline monolayers were synthesized using an atmospheric pressure chemical vapor deposition beforehand. To precisely control the twist angle between two TMDs, a triangular MoSe₂ monolayer was first transferred onto a clean Si substrate (Figure 1A,F) with a 50 nm-thick SiO₂ layer (Figure 1B,G), followed by the precise transfer of another

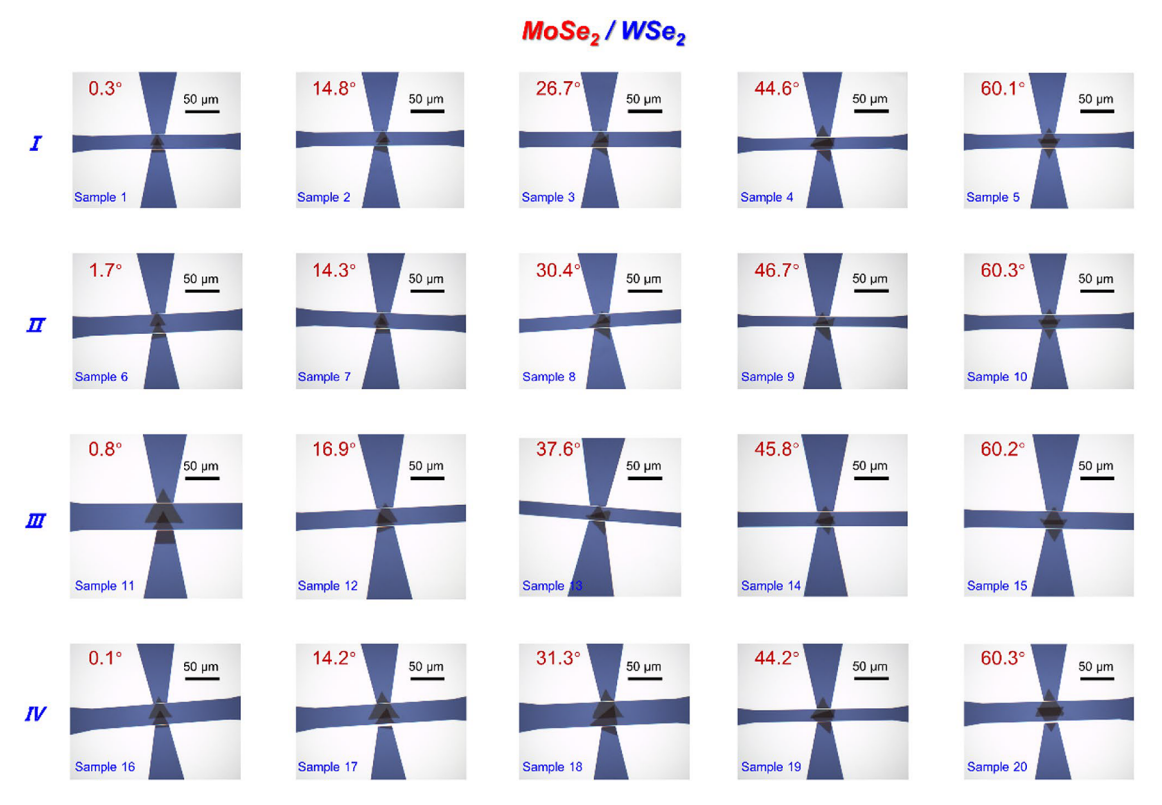


Figure 2. Optical microscope images of multiple stepwise stacked MoSe₂/WSe₂ heterostructure samples. Images I–IV represent five groups of samples with MoSe₂ stacked in front of WSe₂. The twist angles are roughly 0, 15, 30, 45, and 60° in each group.

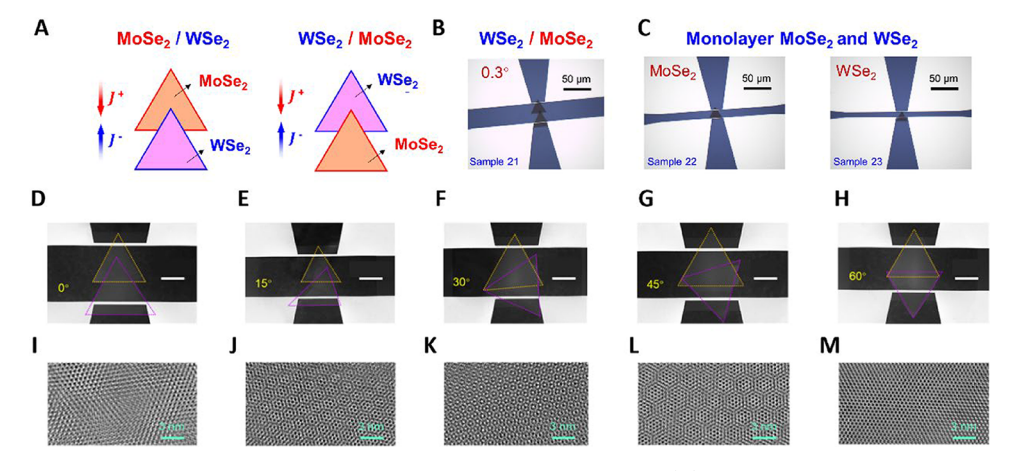


Figure 3. Characterization of the stepwise stacked heterostructures and monolayer TMDs. (A) Schematic diagrams of heterostructure samples with different stacking orientations, i.e., MoSe₂/WSe₂ and WSe₂/MoSe₂. (B) Optical microscope image of the WSe₂/MoSe₂ sample. (C) Optical microscope images of monolayer MoSe₂ and WSe₂, respectively. (D-H) SEM images of the suspended MoSe₂/WSe₂ heterostructure devices with different twist angles after the etching process, where the scale bar is 10 μ m. Yellow and purple dashed triangles represent the single-crystalline MoSe₂ and WSe₂, respectively. (I-M) HR-TEM images depicting the moiré patterns with different twist angles presented in the central overlapping region of the heterobilayer.

triangular WSe₂ monolayer on top with a finely adjusted twist angle (Figure 1C,H). A pair of microprobes (TP-001, tip diameter of 1 μ m) were used to mechanically transfer the TMD monolayer with help of a 200 nm-thick polymethyl methacrylate (PMMA) layer. Precise control of twist angle (precision of up to 0.1°) can be achieved through the meticulous manipulation of two microprobes (video and more details of the transfer process are provided in the Supporting Information (SI)). PMMA layer was removed through immersion into warm acetone and subsequent annealing in a mixed gas flow of Ar and H₂ at 400 °C, 8 h to completely clean

possible contaminations or residues. The cleanliness of transferred TMD samples can be confirmed through the high-resolution transmission electron microscope (HR-TEM) images shown in Figure 3.

A 50 nm-thick H-type Au film sensor (Figure 1I-K) was used to simultaneously measure the phonon and electron transport properties of the heterostructure sample, following our previous work.⁵³ An electron-beam lithography (EBL) was used to precisely deposit Au nanosensor and electrodes on the SiO₂/Si substrate, connecting with the transferred MoSe₂/ WSe₂ heterobilayer sample (Figure 1D,I). To further increase

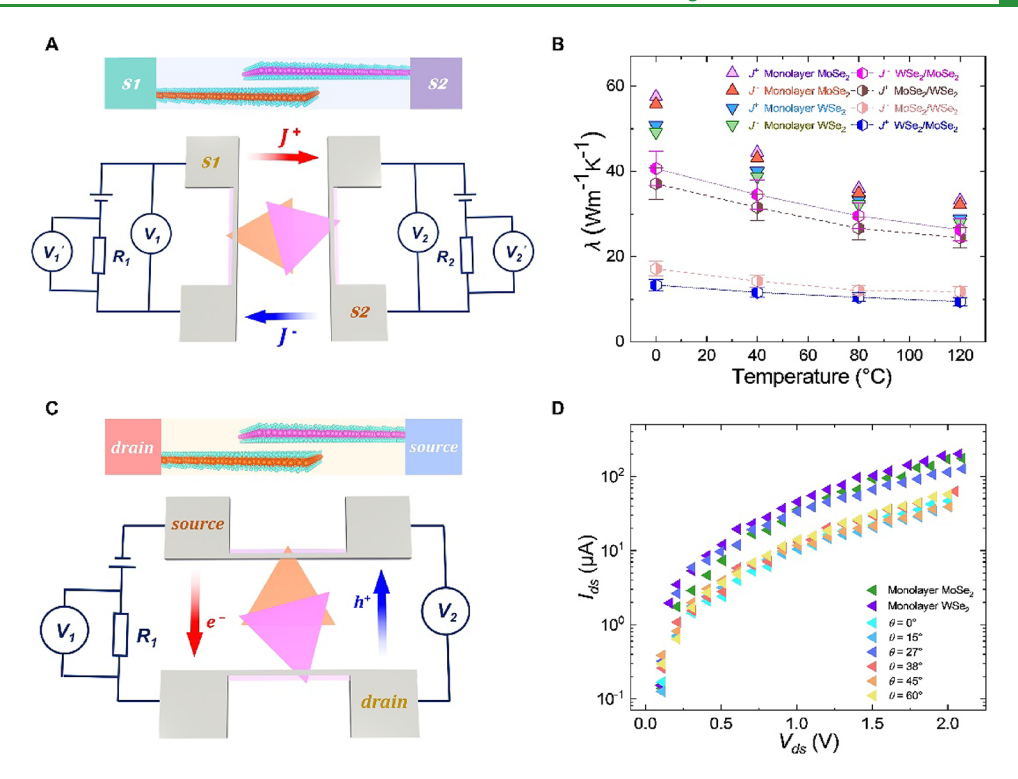


Figure 4. Schematic diagram of thermal and electrical measurement circuits, and comparison of thermal and electrical transport properties between monolayer TMD materials and stepwise stacked heterostructures. (A) Schematic diagram showing the thermal measurement circuit based on the H-type method, involving two electrical circuits, with multimeters V_1 and V_2 used to measure the current in each circuit and multimeters V_1 and V₂ used to measure the voltages across the two Au sensors. The red and blue solid arrows indicate the direction of high and low thermal conductivities from MoSe₂ to WSe₂ and from WSe₂, respectively. (B) Thermal conductivities of monolayer MoSe₂, monolayer WSe₂, and heterostructure samples with two opposite stacking orientations (MoSe₂/WSe₂ and WSe₂/MoSe₂ at $\theta = 0^{\circ}$) under the forward J^{+} and reverse J^{-} heat flow directions at different temperatures. (C) Schematic diagram of the electrical measurement circuit based on the current-voltage method. Multimeters V_1 and V_2 are used to measure the current passing through the stacked heterointerface and the voltage at two sides of the heterostructure, respectively. The red and blue solid arrows indicate the direction of electron and hole movements in the external circuit, respectively. (D) I_{ds} - V_{ds} characteristics of monolayer WSe₂, MoSe₂ and heterostructure devices with different twist angles under the forward bias.

the sensitivity of thermal measurement and minimize the influence of the substrate, the H-type sensing device was fully suspended by etching the SiO₂ and Si below. First, an etching window was defined by using EBL, followed by reactive-ion etching to remove the SiO₂ layer (Figure 1E,J). The supporting Si substrate was subsequently etched by using XeF₂ gas. Finally, the stepwise stacked MoSe₂/WSe₂ heterobilayer was fully suspended between two individual Au nanosensors, forming a H-type sensing device. In order to verify the repeatability and reliability of the measurement results, a total of 46 sensing devices containing monolayer TMD samples and heterobilayer samples with different twist angles and different stacking orientations were fabricated. Here, 20 typical MoSe₂/ WSe₂ samples are shown in Figure 2. One WSe₂/MoSe₂ sample, two MoSe₂, and WSe₂ monolayer samples are shown in Figure 3B,C.

The twist angle θ is defined between two single-crystalline TMDs, where θ = 0° corresponds to the state where triangular MoSe₂ is perfectly aligned with the edges of the triangular WSe₂ layer. In this case, the edges of two layers are parallel to each other. A series of heterobilayer devices were fabricated at different twist angles approximately 0, 15, 30, 45, and 60°, respectively. During fabrication, micron-precision cross-array markers and the EBL system's positioning ability were used to precisely position the heterobilayer samples in the center of two Au nanosensors. Figures 2 and 3 depict the optical and scanning electron microscope (SEM) images of H-type sensing

devices before and after etching, respectively. To investigate the modulation of moiré superlattice by twist angle in the MoSe₂/WSe₂ overlapping region, HR-TEM images were captured and depicted in Figure 3I-M, confirming the cleanness and good quality of transferred heterobilayer samples. Varying twist angles give rise to periodic yet morphologically disparate moiré patterns. When $0^{\circ} < \theta <$ 30°, the period size of moiré superlattice decreases as the twist angle increases, reaching the smallest value at $\theta = 30^{\circ}$. When $30^{\circ} < \theta < 60^{\circ}$, the period size of moiré superlattice increases as the twist angle increases, symmetric with the moiré superlattice when $0^{\circ} < \theta < 30^{\circ}$.

The temperature-dependent thermal conductivities of stepwise stacked MoSe₂/WSe₂ heterobilayers with different interlayer twist angles were measured in different heat flow directions by using the H-type sensor method^{53,54} (Figure 4A). This method is characterized by the use of two Au nanosensors, one acting as the heating source and the other as the temperature response sensor. By switching the roles of two sensors, the direction of heat flow can be easily changed, named J^+ and J^- in the figure. The electrical measurement system includes a precision DC voltage and current source (Japan ADCMT, 6243), two high-accuracy digital multimeters (Keithley 2002, 8½-digits), and a vacuum thermoelectric heating and cooling stage (INSTEC, TP102SV-PM-F8, ± 0.001 K). All the experiments were conducted in a highvacuum chamber with pressure lower than 10⁻³ Pa, where the

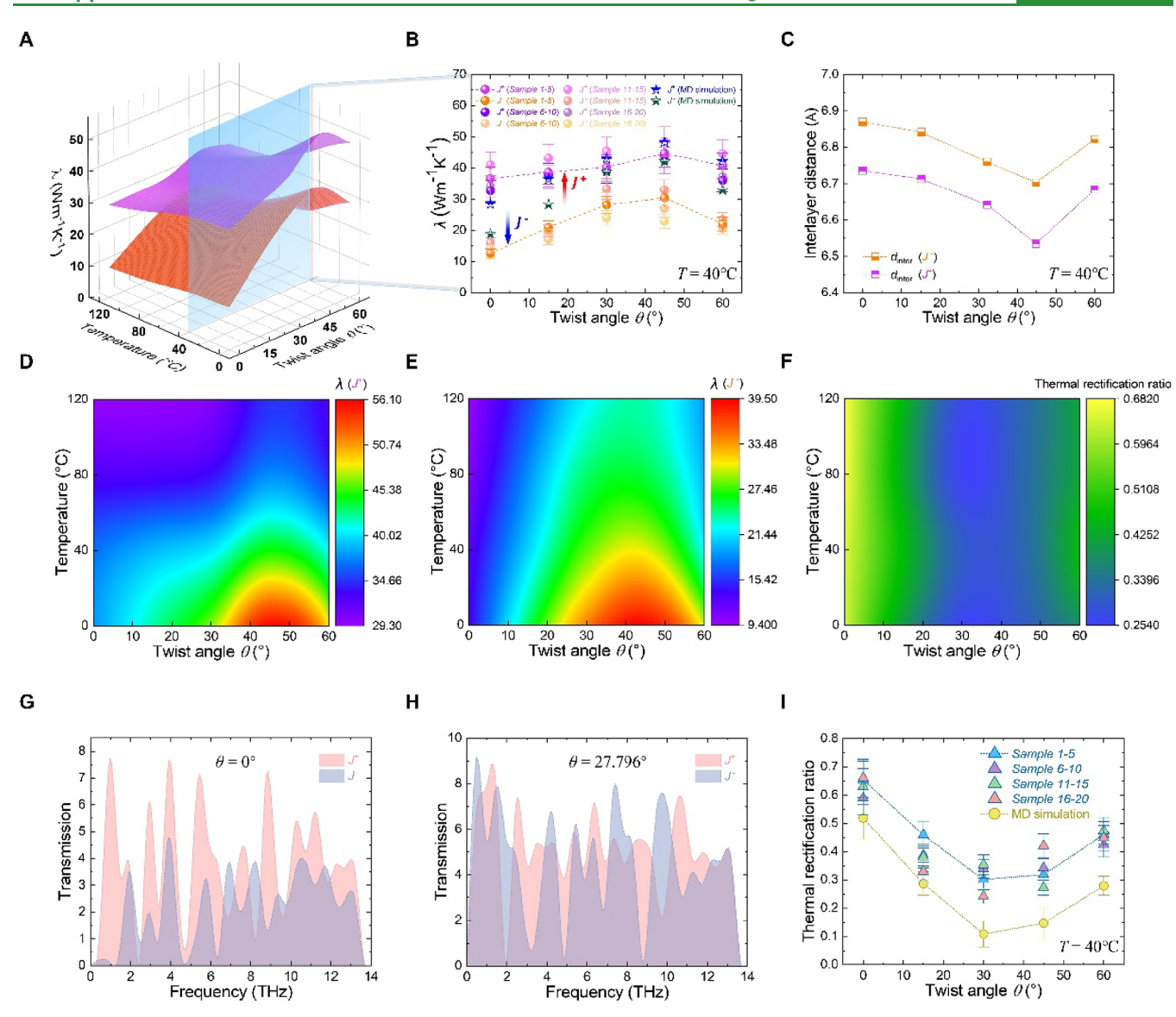


Figure 5. Thermal property characterization of the stepwise stacked $MoSe_2/WSe_2$ van der Waals heterostructures. (A) Experimental results obtained from the heterostructure samples at different temperatures and twist angles. (B) Comparison between the measured thermal conductivities and the NEMD simulation results at T = 40 °C. (C) Interlayer distance (d_{inter}) between $MoSe_2$ and MSe_2 at different twist angles. (D) Variation of the temperature-dependent thermal conductivity with twist angle under forward heat flow J^+ . (E) Variation of the temperature-dependent thermal conductivity with twist angle under reverse heat flow J^- . (F) Variation of the temperature-dependent thermal rectification ratio with twist angle. (G) Calculated phonon transmission coefficient at $\theta = 0^\circ$. (H) Calculated phonon transmission coefficient at $\theta = 27.796^\circ$. (I) Comparison between the measured thermal rectification ratios and the NEMD simulation results at T = 40 °C.

influences of convective heat transfer and thermal radiation could be neglected (the uncertainty analysis can be found in the SI). A three-layer structure is formed at two nanosensor regions. Arranged from top to bottom, the layers are the 50 nm-thick Au sensor, the 0.8 nm-thick monolayer MoSe₂ or WSe₂, and the 50 nm-thick SiO₂ supporting layer, respectively. Significantly, the contact area between Au sensor and TMD monolayer is geometrically far smaller than the area of the heterostructure sample. Hence, due to the relatively large thermal resistance of the heterostructure sample, the contact thermal resistance between the Au sensor and TMD monolayer could be considered negligible (refer to the SI for a detailed discussion). The SiO₂ supporting layer plays a crucial role in providing mechanical support, thereby ensuring the integrity and stability of the heterostructure device. The SiO₂ supporting layer has no influence on the electrical

measurement. Regarding the thermal conductivity measurement of the heterostructure sample, the effect can be eliminated by incorporating the independently measured thermal conductivity of the pure SiO_2 layer into the COMSOL thermal simulation (refer to the SI for detailed analysis).

The measured thermal resistance by H-type sensing device is the overall value of the heterostructure sample between two Au nanosensors, expressed as $R_{\rm total} = R_{\rm MoSe2} + R_{\rm bilayer-in-plane} + R_{\rm bilayer-out-of-plane} + R_{\rm WSe2}$. Here, $R_{\rm bilayer-out-of-plane} = (G \times A_{\rm bilayer})^{-1}$ is the interfacial thermal resistance of the heterobilayer in the overlapping region, where G and $A_{\rm bilayer}$ are the interfacial thermal conductance per unit area and overlapping area; $R_{\rm MoSe2}$, $R_{\rm WSe2}$, and $R_{\rm bilayer}$ in-plane equal $L/(\lambda A_{\rm cross-section})$, where L, λ , and $A_{\rm cross-section}$ are the length, thermal conductivity, and cross-section area of the MoSe₂, WSe₂ monolayer and the overlapped heterobilayer, respectively. According to the

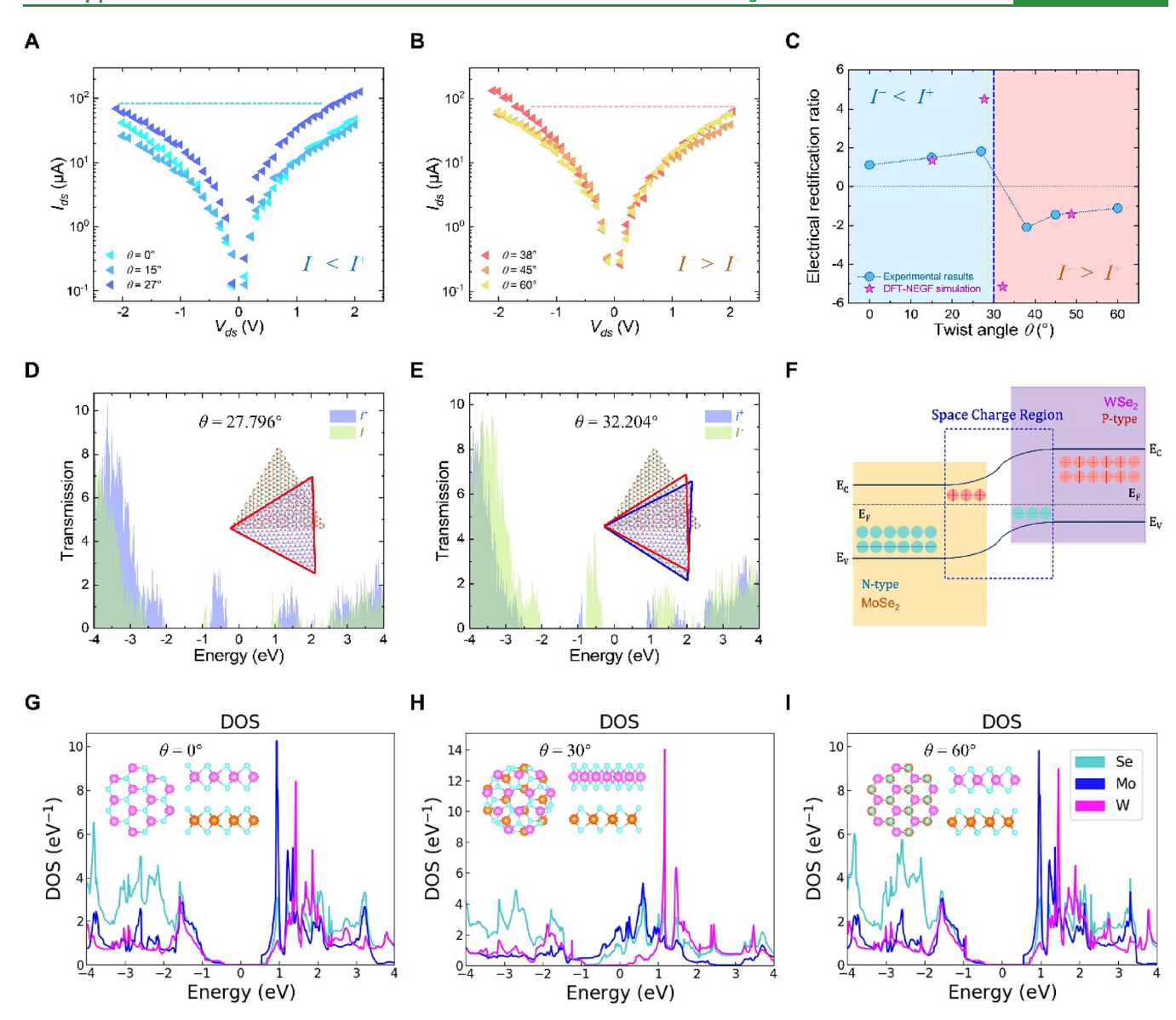


Figure 6. Electrical characterization of the stepwise stacked MoSe₂/WSe₂ heterostructures and DFT simulation results. (A) I_{ds} - V_{ds} curves at different twist angles when θ < 30°. (B) $I_{\rm ds}$ – $V_{\rm ds}$ curves at different twist angles when θ > 30°. (C) Comparison between the measured electrical rectification ratios and that obtained from the density functional theory-nonequilibrium Green's function (DFT-NEGF) simulation results at different twist angles. The vertical dashed line at the critical angle 30° indicates the transition from positive to negative electrical rectification. (D) Calculated electron transmission coefficient at $\theta = 27.796^{\circ}$. (E) Calculated electron transmission coefficient at $\theta = 32.204^{\circ}$. (F) Schematic diagram of the electronic band structure of the MoSe₂/WSe₂ heterostructure. (G-I) Calculated electronic density of states (DOS) at $\theta = 0$, 30, and 60° .

interfacial thermal resistance of TMDs from literature, 47 $R_{\text{bilayer-out-of-plane}}$ is at the magnitude level of 10^3-10^4 K/W, while $R_{\text{bilayer-in-plane}}$ is at the magnitude level of 10⁷ K/W that is approximately 1000 times larger than the former (refer to the SI for details). Hence, the interfacial thermal resistance between MoSe₂ and WSe₂ can be neglected, and the in-plane thermal conductivity of heterobilayer plays a dominant role in the observed thermal rectification behavior.

By simply changing the external electrical circuit, the electrical transport properties can be measured on the sample (Figure 4C). Figure 4B,D compares the different thermal conductivities and $I_{\rm ds}{-}V_{\rm ds}$ curves between the pure monolayer MoSe₂, WSe₂, and stepwise stacked heterostructures. It is seen that the thermal conductivities of monolayer TMD materials remain nearly the same in both J^+ and J^- heat flow directions, which indicates a negligible thermal rectification effect. In contrast, the thermal conductivities of heterostructure samples depend on the heat flow direction, exhibiting a strong thermal rectification effect. It is confirmed that higher thermal conductivity always occurs when heat flows from MoSe2 to WSe_2 (\int^+ direction in $MoSe_2/WSe_2$ and \int^- direction in WSe_2/VSe_2) MoSe₂). A four-probe method was used to measure the $I_{\rm ds}$ – $V_{\rm ds}$ curve of pure monolayer TMDs and heterostructure samples at room temperature (T = 25 °C). Due to the additional electron-electron and electron-boundary scattering at the heterointerface, the current of the heterostructure sample is lower than that of the monolayers. It is demonstrated that the twist angle effectively modulates electrical transport through the heterointerface. The electrical current at $\theta \approx 30^{\circ}$ is significantly larger than that at $\theta \approx 0^{\circ}$.

Thermal Rectification Measurements and Device **Simulations.** Figure 5A represents all of the measured thermal conductivities of heterostructure samples in Figures 2 and 3 at different twist angles and temperatures in both forward and reverse heat flow directions. Figure 5A reveals that the twist angle θ considerably affects the thermal conductivities of the stepwise stacked MoSe₂/WSe₂ heterostructures, confirming that the twist-controlled moiré superlattice causes substantial changes in the in-plane phonon transport. Fullatom nonequilibrium molecular dynamics (NEMD) simulations were conducted at 40 °C to understand the mechanism. As shown in Figure 5B, the simulation results align well with the experimental results. Notably, the thermal conductivity reaches a maximum value at approximately $\theta = 45^{\circ}$, at which the interlayer distance d_{inter} between $MoSe_2$ and WSe_2 is minimal (Figure 5C). Furthermore, the variation of d_{inter} with a twist angle at 40 °C represents an opposite trend of thermal conductivity, indicating that a small interlayer distance strengthens the interlayer interactions and improves the inplane phonon transport. Further results of the phonon transmission coefficient (Figure S4) reveal that for the 30 and 45° twisted configurations, which exhibit stronger interlayer coupling, the transmission coefficient is markedly enhanced within the 2-6 THz frequency range, whereas phonon transmission at other frequencies remains largely unaffected. This indicates that these specific twist angles introduce additional phonon transmission channels, thereby improving the overall heat transport efficiency.

Additionally, Figure 5D,E reveals that the variations in the thermal conductivity become more pronounced with varying twist angle under the reverse heat flow than under the forward heat flow. Such difference in thermal conductivities suggests that the thermal rectification ratio (TRR) of the heterostructure sample is influenced by the twist angle, i.e., the interlayer interactions at different moiré superlattices. Figure 5F shows the TRR at different temperatures and twist angles from the experimental results. It is seen that temperature has little effect on the TRR, whereas twist angle θ plays a crucial role in modulating thermal rectification. The TRR is the highest when θ equals 0 and 60°, and relatively lower when θ is in a range from 15 to 45°. Figure 5I reveals that the trend of TRR from the NEMD simulation is consistent with that measured in the experiment. Specifically, the TRR decreases as the twist angle increases from 0 to 30° and reaches the minimal value at 30°, after that the TRR again increases from 30 to 60°. To understand the underlying mechanism, the phonon transmission coefficient through the stepwise stacked heterobilayer was computed at different twist angles in both J^+ and $J^$ heat flow directions. The intensities of spectral distinct peaks in Figure 5G show a remarkable difference between the cases of J^+ and J^- at $\theta = 0^\circ$, confirming the occurrence of thermal rectification. In contrast, at $\theta \approx 27.8^{\circ}$, the intensities of the low-frequency phonon peaks for both I^+ and I^- are enhanced, with a more pronounced increase in the transmission coefficient observed in the opposite heat flow direction (\mathcal{T}) . This reduces the asymmetry in transmission capacity between the two directions, thereby suppressing the thermal rectification effect. This demonstrates that the in-plane phonon transport in heterobilayers is highly sensitive to the twistcontrolled moiré superlattice, and the phonon transmissivity depends on the heat flow direction. It is crucial to emphasize that the observed minimum in the TRR is fundamentally distinct from the so-called "thermal magic angle", which is defined as the twist angle corresponding to the local minimum in thermal conductivity of twisted bilayer graphene.³⁷ Our

findings reveal that distinct twist angles are necessary to independently optimize thermal conduction (maximizing λ) and directional thermal control (maximizing TRR).

Electrical Characterization of Heterostructures and **DFT Simulations.** I_{ds} – V_{ds} curves of MoSe₂/WSe₂ samples with different twist angles were measured at zero gate voltage and room temperature (T = 25 °C) (Figure 6A,B). The results indicate that the current responses to the forward and reverse biases are asymmetric, similar to those of the covalent P-Ntype heterostructures, such as monolayer MoSe₂/WSe₂ lateral heterojunctions.⁵⁴ However, the asymmetry of electrical rectification in the van der Waals heterobilayer is significantly weaker than that of covalent lateral heterojunctions. As shown in Figure 6F, the N-type MoSe₂ and P-type WSe₂ form a natural P-N junction solely owing to the weak van der Waals interactions between layers. According to the diode effect principle, a depletion region forms at the heterointerface owing to the diffusion of carriers. When a reverse bias is applied, this depletion region generates an energy barrier, hindering the migration of the carriers. In the lateral heterostructures, the width of the depletion region is commensurate with the geometric dimensions of the materials flanking the interface.⁵⁵ In the stacked van der Waals heterostructure, the thicknesses of the P-type and N-type materials, being monolayer WSe2 and MoSe_{2,} respectively, exert an effective limitation on the width of the depletion region. This significantly weakens the energy barrier at the heterointerface in contrast with the covalent lateral heterojunctions and causes weak electrical rectification behaviors.

Interestingly, Figure 6C shows that the electrical rectification of the MoSe₂/WSe₂ heterobilayer undergoes a fierce change from positive to negative at the critical twist angle 30°, which corresponds to the minimum period of moiré superlattice. This dependence of the electrical rectification ratio on the twist angle is consistent with the I_{ds} - V_{ds} curve simulation results conducted by DFT-NEGF simulations. To further clarify the mechanism, the electronic band structure and DOS of the unit cell in the moiré superlattice were computed at $\theta = 0$, 30, and 60°, as shown in Figure 6G–I, respectively (details of the band structure can be found in the SI). The DOS results indicate that as the twist angle increases from 0 to 30°, the difference in the peak densities obtained from Mo and W atoms gradually increases, enhancing the electrical rectification effect of the heterostructure. When the twist angle θ exceeds the critical value of 30°, the direction of electrical asymmetry reverses (Figure 6A–C). Specifically, when θ < 30°, the forward current is larger than the reverse current, yielding a positive rectification ratio. When $\theta > 30^{\circ}$, the forward current is smaller than the reverse current, yielding a negative rectification ratio. Furthermore, the electron transmission coefficients of the heterobilayer devices were computed, and the blue and green peaks represent the transmission coefficients under the forward and reverse biases, respectively. At $\theta \approx 27^{\circ}$, the transmission coefficient under forward bias is significantly larger than that under the reverse bias, confirming positive electrical rectification, as shown in Figure 6D. In contrast, at $\theta \approx 32^{\circ}$, the transmission coefficient under forward bias is smaller than that under the reverse bias, so the direction of electrical asymmetry reverses, as shown in Figure 6E. The simulation results agree well with the experimental data.

CONCLUSION

In order to investigate the coexistent modulation of the twistcontrolled moiré superlattice on the electron and phonon transport, stepwise stacked van der Waals heterostructures constructed by single-crystalline MoSe₂ and WSe₂ were fabricated. The period of moiré superlattice can be continuously tuned by changing the twist angle between two layers. A significant in-plane thermal rectification behavior is observed and the rectification ratio decreases from 65 to 30% as the moiré superlattice period declines with the twist angle increasing from 0 to 30°. Meanwhile, the electrical rectification ratio increases from 100 to 200%. Interestingly, at the critical value of 30° corresponding to the minimum period of moiré superlattice, the TRR reaches the minimum value while the electrical rectification goes through a violent transition from the positive state to the negative state. This demonstrates that the moiré-controlled heterointerface provokes different rectifying responses for phonons and electrons. These findings significantly advance our understanding of phonon and electron transport characteristics at twisted van der Waals interfaces, offering a new paradigm for moiré engineering. The synergistic manipulation of phonon and electron channels not only expands the design space for next-generation functional materials, but also establishes concrete implementation pathways for high-efficiency thermoelectric energy conversion, intelligent thermal management, and reconfigurable logic devices.

METHODS

Calculation of Thermal Conductivity, TRR, Phonon Transmission Coefficient Spectrum, and Vibrational DOS. Molecular dynamics simulations were conducted using the open-source LAMMPS⁵⁶ package. A stepwise stacked MoSe₂/WSe₂ van der Waals heterostructure (approximately 7000 atoms) was constructed via the stepwise stacking of monolayer MoSe₂ and WSe₂, which were twisted relative to each other at designated angles. The interlayer twist angles investigated were 0, 15.18, 27.796, 44.82, and 60°. The covalent interactions within these heterostructures were described using the Stillinger-Weber (SW) potential, whereas the van der Waals interactions were captured by the Lennard-Jones (LJ) potential⁵⁸ (refer to the SI for details). The SW and LJ potentials have been extensively validated and widely applied in thermal transport calculations for systems with structures analogous to ours. 34,59 Owing to the nonperiodic nature of the models in the x and y dimensions, fixed boundary conditions were imposed along these axes. Additionally, periodic boundary conditions were applied along the z-axis to simulate an infinite extension in the out-of-plane direction. The time step for propagating the equations of motion was set as 0.5 fs. The calculated system was initially relaxed to its energetic minimum using the conjugate gradient algorithm. Subsequently, at a thermodynamic state of 313 K, the system was subjected to a relaxation protocol consisting of an initial process for 250 ps under the NPT ensemble and a subsequent 250 ps of relaxation under the NVT ensemble. Then, the NVE ensemble was implemented within the interior regions for 8 ns to enable the system to converge to a stable thermodynamic state with the heat source and sink maintained at temperatures of T = 363 and 263 K, respectively. Thermal conductivity and heat flow were computed using data from the final 3 ns of the simulation. All the reported results represent the average of six independent calculations, and each simulation was initiated using a distinct random seed to generate the initial velocities. The TRR can be determined using the formula $\eta = (J^+ - J^-)/J^-$, where J^+ and $J^$ denote the directions of high and low heat flows, respectively. The results of the NEMD simulations were used to calculate the phonon transmission coefficients and phonon vibrational DOS⁶⁰⁻⁶²

considering the forces and velocities of the atoms (for details, refer to the SI).

Calculation of the Electron Transmission Coefficient Spectrum, I-V Characteristics, Electronic Band Structure, and DOS. The model of the stepwise stacked MoSe₂/WSe₂ moiré heterostructure was composed of stepwise stacked monolayer MoSe₂ and WSe2 at specific twist angles. The size of the calculated model was 15×70 Å along the x and y directions. The maximum force between the atoms was 0.01 eV/Å. The thickness of the vacuum layer in the zdirection was more than 15 Å, accurately reflecting the properties of the monolayer. All the calculations were implemented using the Quantum ATK package. 63 First, the electron transmission spectrum was calculated. Subsequently, the currents at different bias voltages were calculated using the Landauer-Buttiker formula, 64 yielding the conductance of the calculated system in terms of the electron transmission coefficient. The NEGF method⁶⁵ was used to selfconsistently calculate the I-V characteristics; the NEGF method has been widely used to analyze electron transport. We used the semiempirical extended Hückel theory (EHT)66 basis set with a density mesh cutoff of 10 hartree. Owing to its high computational efficiency,⁶⁷ EHT is particularly suited for modeling complex systems and is often utilized to accelerate the computation of electron transport properties. 68,69 All of the Hamiltonian elements were set using the Hoffman parameter and calculated using the Wolfsberg weighting scheme. Further, the recursion method was used to calculate the self-energy. The k-point grid of the Brillouin zone was 5 \times 5 \times 150 along the x, y, and z directions on a Monkhorst-Pack grid with unpolarized spin (Γ -centered). The maximum interaction range was 10 Å, and the electron temperature was 300 K.

The electronic band structure and DOS were calculated based on the unit cell. We used the linear combination of atomic orbitals⁷ basis set with a density mesh cutoff of 75 hartree. The exchangecorrelation potential was described using the hybrid generalized gradient approximation functional, parametrized using the Heyd-Scuseria-Ernzerhof (HSE)⁷¹ hybrid functional. The HSE functional not only exhibits enhanced computational efficiency over traditional hybrid functionals⁷² but also provides remarkable accuracy in predicting essential material properties, including band gaps, surpassing pure DFT approaches. Further, the recursion method was used to calculate the self-energy. To better describe the weak van der Waals interactions, the DFT-D2 empirical correction method proposed by Grimme⁷⁴ was adopted. The k-point grid of the Brillouin zone was $8 \times 8 \times 1$ along the x, y, and z directions on the Monkhorst-Pack grid with unpolarized spin (Γ -centered). The energy convergence criterion of the self-consistent iterative calculation was 10^{-4} eV.

ASSOCIATED CONTENT

Supporting Information

The Supporting Information is available free of charge at https://pubs.acs.org/doi/10.1021/acsami.5c11910.

Fabrication methods for materials and heterostructures device; simulation methods; uncertainty analysis of experimental data (PDF)

Video of transfer process (MP4)

AUTHOR INFORMATION

Corresponding Authors

Haidong Wang - Key Laboratory for Thermal Science and Power Engineering of Ministry of Education, Department of Engineering Mechanics, Tsinghua University, Beijing 100084, China; orcid.org/0000-0001-8933-2279;

Email: hdwang@tsinghua.edu.cn

Bingyang Cao - Key Laboratory for Thermal Science and Power Engineering of Ministry of Education, Department of Engineering Mechanics, Tsinghua University, Beijing 100084, China; orcid.org/0000-0003-3588-972X; Email: caoby@tsinghua.edu.cn

Authors

- Yaohong Zhou Key Laboratory for Thermal Science and Power Engineering of Ministry of Education, Department of Engineering Mechanics, Tsinghua University, Beijing 100084, China; ⊚ orcid.org/0000-0001-7094-3512
- Siqi Xie Key Laboratory for Thermal Science and Power Engineering of Ministry of Education, Department of Engineering Mechanics, Tsinghua University, Beijing 100084, China; orcid.org/0009-0002-2626-3004
- Jie Zheng Key Laboratory for Thermal Science and Power Engineering of Ministry of Education, Department of Engineering Mechanics, Tsinghua University, Beijing 100084, China
- Hongxin Zhu Key Laboratory for Thermal Science and Power Engineering of Ministry of Education, Department of Engineering Mechanics, Tsinghua University, Beijing 100084, China

Complete contact information is available at: https://pubs.acs.org/10.1021/acsami.5c11910

Author Contributions

*H.W., Y.Z., and S.X. contributed equally to this paper as the first authors. H.W. and B.C. supervised the project. H.W. and H.Z. prepared the CVD grown single-crystalline TMD samples and fabricated the suspended sensing devices for thermal and electrical measurement. H.W. and Y.Z. preformed the electrical and thermal property measurements and data analysis. Y.Z., S.X., and J.Z. performed molecular dynamics simulation and finite element analysis. Y.Z. preformed high-resolution transmission electron microscope experiment. Y.Z. and H.W. wrote the manuscript with the participation of all authors. All authors participated in the discussion of the results and in the revision of the manuscript.

Notes

The authors declare no competing financial interest.

ACKNOWLEDGMENTS

This work was supported by the National Key Research and Development Program of China (Grant No. 2023YFB4404100) and National Natural Science Foundation of China (Grant Nos. 52425601, 52327809, 52276072).

ABBREVIATIONS

2D,two-dimensional; TMD,transition metal dichalcogenide; PMMA,polymethyl methacrylate; HR-TEM,high-resolution transmission electron microscope; EBL,electron-beam lithography; SEM,scanning electron microscope; NEMD,nonequilibrium molecular dynamics; TRR,thermal rectification ratio; DFT-NEGF,density functional theory-nonequilibrium Green's function; DOS,density of states

REFERENCES

- (1) Novoselov, K. S.; Jiang, D.; Schedin, F.; Booth, T. J.; Khotkevich, V. V.; Morozov, S. V.; Geim, A. K. Two-Dimensional Atomic Crystals. *Proc. Natl. Acad. Sci. U.S.A.* **2005**, *102* (30), 10451–10453.
- (2) Chamlagain, B.; Withanage, S. S.; Johnston, A. C.; Khondaker, S. I. Scalable Lateral Heterojunction by Chemical Doping of 2D TMD Thin Films. *Sci. Rep.* **2020**, *10* (1), 12970.
- (3) Chen, S.; Liang, Z.; Miao, J.; Yu, X.-L.; Wang, S.; Zhang, Y.; Wang, H.; Wang, Y.; Cheng, C.; Long, G.; Wang, T.; Wang, L.;

- Zhang, H.; Chen, X. Infrared Optoelectronics in Twisted Black Phosphorus. *Nat. Commun.* **2024**, *15* (1), 8834.
- (4) Peng, L.; Xiong, P.; Ma, L.; Yuan, Y.; Zhu, Y.; Chen, D.; Luo, X.; Lu, J.; Amine, K.; Yu, G. Holey Two-Dimensional Transition Metal Oxide Nanosheets for Efficient Energy Storage. *Nat. Commun.* **2017**, 8 (1), 15139.
- (S) Liu, Y.; Guo, J.; Zhu, E.; Liao, L.; Lee, S.-J.; Ding, M.; Shakir, I.; Gambin, V.; Huang, Y.; Duan, X. Approaching the Schottky-Mott Limit in van Der Waals Metal-Semiconductor Junctions. *Nature* **2018**, 557 (7707), 696–700.
- (6) Mak, K. F.; Lee, C.; Hone, J.; Shan, J.; Heinz, T. F. Atomically Thin MoS₂: A New Direct-Gap Semiconductor. *Phys. Rev. Lett.* **2010**, 105 (13), No. 136805.
- (7) Liu, X.; Hersam, M. C. 2D Materials for Quantum Information Science. *Nat. Rev. Mater.* **2019**, 4 (10), 669–684.
- (8) Zheliuk, O.; Kreminska, Y.; Fu, Q.; Pizzirani, D.; Ammerlaan, E. L. Q. N.; Wang, Y.; Hameed, S.; Wan, P.; Peng, X.; Wiedmann, S.; Liu, Z.; Ye, J.; Zeitler, U. Quantum Hall Effect in a CVD-Grown Oxide. *Nat. Commun.* **2024**, *15* (1), 10052.
- (9) Busool, R.; Haick, H. Nanomaterial-based Transistors for Chemical and Biological Sensing. *Organic and Inorganic Materials Based Sensors* **2024**, *2*, 479–493.
- (10) Sharma, N.; Islam, R.; Mudila, H.; Kumar, A. In 2D Materials: Sensing Applications; Springer: 2024; pp 129–141.
- (11) Bresnehan, M. S.; Hollander, M. J.; Wetherington, M.; LaBella, M.; Trumbull, K. A.; Cavalero, R.; Snyder, D. W.; Robinson, J. A. Integration of Hexagonal Boron Nitride with Quasi-Freestanding Epitaxial Graphene: Toward Wafer-Scale. *High-Performance Devices*. ACS Nano 2012, 6 (6), 5234–5241.
- (12) Bertolazzi, S.; Krasnozhon, D.; Kis, A. Nonvolatile Memory Cells Based on MoS₂ /Graphene Heterostructures. *ACS Nano* **2013**, 7 (4), 3246–3252.
- (13) Regan, E. C.; Wang, D.; Jin, C.; Bakti Utama, M. I.; Gao, B.; Wei, X.; Zhao, S.; Zhao, W.; Zhang, Z.; Yumigeta, K.; Blei, M.; Carlström, J. D.; Watanabe, K.; Taniguchi, T.; Tongay, S.; Crommie, M.; Zettl, A.; Wang, F. Mott and Generalized Wigner Crystal States in WSe₂/WS₂ Moiré Superlattices. *Nature* **2020**, *579* (7799), 359–363.
- (14) Wang, L.-F.; Ma, T.-B.; Hu, Y.-Z.; Zheng, Q.; Wang, H.; Luo, J. Superlubricity of Two-Dimensional Fluorographene/MoS₂ Heterostructure: A First-Principles Study. *Nanotechnology* **2014**, 25 (38), No. 385701.
- (15) Jin, C.; Regan, E. C.; Yan, A.; Iqbal Bakti Utama, M.; Wang, D.; Zhao, S.; Qin, Y.; Yang, S.; Zheng, Z.; Shi, S.; Watanabe, K.; Taniguchi, T.; Tongay, S.; Zettl, A.; Wang, F. Observation of Moiré Excitons in WSe₂/WS₂ Heterostructure Superlattices. *Nature* **2019**, 567 (7746), 76-80.
- (16) Jiang, J.-W.; Park, H. S. Mechanical Properties of MoS₂/Graphene Heterostructures. *Appl. Phys. Lett.* **2014**, 105 (3), No. 033108
- (17) Zeng, H.; Chen, R.; Yao, G. Tunable Electronic Properties and Potential Applications of 2D GeP/Graphene van Der Waals Heterostructure. *Adv. Electron. Mater.* **2020**, *6* (3), No. 1901024.
- (18) Alcaraz Iranzo, D.; Nanot, S.; Dias, E. J. C.; Epstein, I.; Peng, C.; Efetov, D. K.; Lundeberg, M. B.; Parret, R.; Osmond, J.; Hong, J.-Y.; Kong, J.; Englund, D. R.; Peres, N. M. R.; Koppens, F. H. L. Probing the Ultimate Plasmon Confinement Limits with a van Der Waals Heterostructure. *Science* **2018**, *360* (6386), 291–295.
- (19) Woessner, A.; Lundeberg, M. B.; Gao, Y.; Principi, A.; Alonso-González, P.; Carrega, M.; Watanabe, K.; Taniguchi, T.; Vignale, G.; Polini, M.; Hone, J.; Hillenbrand, R.; Koppens, F. H. L. Highly Confined Low-Loss Plasmons in Graphene-Boron Nitride Heterostructures. *Nat. Mater.* **2015**, *14* (4), 421–425.
- (20) Bandurin, D. A.; Svintsov, D.; Gayduchenko, I.; Xu, S. G.; Principi, A.; Moskotin, M.; Tretyakov, I.; Yagodkin, D.; Zhukov, S.; Taniguchi, T.; Watanabe, K.; Grigorieva, I. V.; Polini, M.; Goltsman, G. N.; Geim, A. K.; Fedorov, G. Resonant Terahertz Detection Using Graphene Plasmons. *Nat. Commun.* **2018**, *9* (1), 5392.
- (21) Britnell, L.; Ribeiro, R. M.; Eckmann, A.; Jalil, R.; Belle, B. D.; Mishchenko, A.; Kim, Y.-J.; Gorbachev, R. V.; Georgiou, T.; Morozov,

- S. V.; Grigorenko, A. N.; Geim, A. K.; Casiraghi, C.; Neto, A. H. C.; Novoselov, K. S. Strong Light-Matter Interactions in Heterostructures of Atomically Thin Films. *Science* **2013**, *340* (6138), 1311–1314.
- (22) Mudd, G. W.; Svatek, S. A.; Hague, L.; Makarovsky, O.; Kudrynskyi, Z. R.; Mellor, C. J.; Beton, P. H.; Eaves, L.; Novoselov, K. S.; Kovalyuk, Z. D.; Vdovin, E. E.; Marsden, A. J.; Wilson, N. R.; Patanè, A. High Broad-band Photoresponsivity of Mechanically Formed InSe–Graphene van Der Waals Heterostructures. *Adv. Mater.* **2015**, 27 (25), 3760–3766.
- (23) Wu, X.; Han, Q. Phonon Thermal Transport across Multilayer Graphene/Hexagonal Boron Nitride van Der Waals Heterostructures. ACS Appl. Mater. Interfaces 2021, 13 (27), 32564–32578.
- (24) Kang, J.; Li, J.; Li, S.-S.; Xia, J.-B.; Wang, L.-W. Electronic Structural Moiré Pattern Effects on MoS₂ /MoSe₂ 2D Heterostructures. *Nano Lett.* **2013**, *13* (11), 5485–5490.
- (25) Kim, K.; DaSilva, A.; Huang, S.; Fallahazad, B.; Larentis, S.; Taniguchi, T.; Watanabe, K.; LeRoy, B. J.; MacDonald, A. H.; Tutuc, E. Tunable Moiré Bands and Strong Correlations in Small-Twist-Angle Bilayer Graphene. *Proc. Natl. Acad. Sci. U.S.A.* **2017**, *114* (13), 3364–3369.
- (26) Balents, L.; Dean, C. R.; Efetov, D. K.; Young, A. F. Superconductivity and Strong Correlations in Moiré Flat Bands. *Nat. Phys.* **2020**, *16* (7), 725–733.
- (27) Carr, S.; Massatt, D.; Fang, S.; Cazeaux, P.; Luskin, M.; Kaxiras, E. Twistronics: Manipulating the Electronic Properties of Two-Dimensional Layered Structures through Their Twist Angle. *Phys. Rev. B* **2017**, *95* (7), No. 075420.
- (28) Cao, Y.; Fatemi, V.; Fang, S.; Watanabe, K.; Taniguchi, T.; Kaxiras, E.; Jarillo-Herrero, P. Unconventional Superconductivity in Magic-Angle Graphene Superlattices. *Nature* **2018**, *556* (7699), 43–50.
- (29) Cao, Y.; Fatemi, V.; Demir, A.; Fang, S.; Tomarken, S. L.; Luo, J. Y.; Sanchez-Yamagishi, J. D.; Watanabe, K.; Taniguchi, T.; Kaxiras, E.; Ashoori, R. C.; Jarillo-Herrero, P. Correlated Insulator Behaviour at Half-Filling in Magic-Angle Graphene Superlattices. *Nature* **2018**, 556 (7699), 80–84.
- (30) Xian, L.; Claassen, M.; Kiese, D.; Scherer, M. M.; Trebst, S.; Kennes, D. M.; Rubio, A. Realization of Nearly Dispersionless Bands with Strong Orbital Anisotropy from Destructive Interference in Twisted Bilayer MoS₂. *Nat. Commun.* **2021**, *12* (1), 5644.
- (31) Angeli, M.; MacDonald, A. H. Γ Valley Transition Metal Dichalcogenide Moiré Bands. *Proc. Natl. Acad. Sci. U. S. A.* **2021**, *118* (10), No. e2021826118.
- (32) Naik, M. H.; Jain, M. Ultraflatbands and Shear Solitons in Moiré Patterns of Twisted Bilayer Transition Metal Dichalcogenides. *Phys. Rev. Lett.* **2018**, *121* (26), No. 266401.
- (33) Xian, L.; Kennes, D. M.; Tancogne-Dejean, N.; Altarelli, M.; Rubio, A. Multi-Flat Bands and Strong Correlations in Twisted Bilayer Boron Nitride. *Nano Lett.* **2019**, *19* (8), 4934–4940.
- (34) Ni, G. X.; Wang, H.; Jiang, B.-Y.; Chen, L. X.; Du, Y.; Sun, Z. Y.; Goldflam, M. D.; Frenzel, A. J.; Xie, X. M.; Fogler, M. M.; Basov, D. N. Soliton Superlattices in Twisted Hexagonal Boron Nitride. *Nat. Commun.* **2019**, *10* (1), 4360.
- (35) Mandal, S.; Maity, I.; Das, A.; Jain, M.; Maiti, P. K. Tunable Lattice Thermal Conductivity of Twisted Bilayer MoS₂. *Phys. Chem. Chem. Phys.* **2022**, 24 (22), 13860–13868.
- (36) Lin, M.-L.; Tan, Q.-H.; Wu, J.-B.; Chen, X.-S.; Wang, J.-H.; Pan, Y.-H.; Zhang, X.; Cong, X.; Zhang, J.; Ji, W.; Hu, P.-A.; Liu, K.-H.; Tan, P.-H. Moiré Phonons in Twisted Bilayer MoS₂. *ACS Nano* **2018**, *12* (8), 8770–8780.
- (37) Cheng, Y.; Fan, Z.; Zhang, T.; Nomura, M.; Volz, S.; Zhu, G.; Li, B.; Xiong, S. Magic Angle in Thermal Conductivity of Twisted Bilayer Graphene. *Materials Today Physics* **2023**, *35*, No. 101093.
- (38) Li, L.; Lin, K.; Zhang, L. Twist Angle-Dependent Interface Thermal Conductance in MoS₂ Bilayers. *J. Electron. Mater.* **2022**, *51* (6), 2949–2955.
- (39) Yang, F.; Song, B. Near-Field Thermal Transport between Two Identical Twisted Bilayer Graphene Sheets Separated by a Vacuum Gap. *Phys. Rev. B* **2021**, *103* (23), No. 235415.

- (40) Ren, W.; Ouyang, Y.; Jiang, P.; Yu, C.; He, J.; Chen, J. The Impact of Interlayer Rotation on Thermal Transport Across Graphene/Hexagonal Boron Nitride van Der Waals Heterostructure. *Nano Lett.* **2021**, 21 (6), 2634–2641.
- (41) Meng, K.; An, M.; Chen, D.; Chi, C.; Li, S.; Song, J.; Zhang, G. Unveiling the Magic of Twist Angle: Thermal Transport in Two-Dimensional Graphene/MoS₂/Graphene Heterostructures. *Surfaces and Interfaces* **2024**, *51*, No. 104525.
- (42) Jiang, W.; Liang, T.; Bu, H.; Xu, J.; Ouyang, W. Moiré-Driven Interfacial Thermal Transport in Twisted Transition Metal Dichalcogenides. ACS Nano 2025, 19, 16287—16296.
- (43) Eriksson, F.; Fransson, E.; Linderälv, C.; Fan, Z.; Erhart, P. Tuning the Through-Plane Lattice Thermal Conductivity in van Der Waals Structures through Rotational (Dis)Ordering. ACS Nano 2023, 17 (24), 25565–25574.
- (44) Jiang, W.; Liang, T.; Xu, J.; Ouyang, W. Twist-Dependent Anisotropic Thermal Conductivity in Homogeneous MoS₂ Stacks. *Int. J. Heat Mass Transfer* **2023**, *217*, No. 124662.
- (45) Ouyang, W.; Qin, H.; Urbakh, M.; Hod, O. Controllable Thermal Conductivity in Twisted Homogeneous Interfaces of Graphene and Hexagonal Boron Nitride. *Nano Lett.* **2020**, *20* (10), 7513–7518.
- (46) Zhang, L.; Zhong, Y.; Li, X.; Park, J.-H.; Song, Q.; Li, L.; Guo, L.; Kong, J.; Chen, G. Effect of Twist Angle on Interfacial Thermal Transport in Two-Dimensional Bilayers. *Nano Lett.* **2023**, 23 (17), 7790–7796.
- (47) Kim, S. E.; Mujid, F.; Rai, A.; Eriksson, F.; Suh, J.; Poddar, P.; Ray, A.; Park, C.; Fransson, E.; Zhong, Y.; Muller, D. A.; Erhart, P.; Cahill, D. G.; Park, J. Extremely Anisotropic van Der Waals Thermal Conductors. *Nature* **2021**, 597 (7878), 660–665.
- (48) Yang, F.; Zhou, W.; Zhang, Z.; Huang, X.; Zhang, J.; Liang, N.; Yan, W.; Wang, Y.; Ding, M.; Guo, Q.; Han, Y.; Liu, T.-H.; Liu, K.; Zheng, Q.; Song, B. Ultrahigh Thermal Conductance across Superlubric Interfaces in Twisted Graphite. *Phys. Rev. Lett.* **2025**, 134 (14), No. 146302.
- (49) Ren, W.; Chen, J.; Zhang, G. Phonon physics in twisted two-dimensional materials. *Appl. Phys. Lett.* **2022**, *121* (14), 140501.
- (50) Antidormi, A.; Royo, M.; Rurali, R. Electron and Phonon Transport in Twisted Graphene Nanoribbons. *J. Phys. D: Appl. Phys.* **2017**, *50* (23), 234005.
- (51) Ray, N.; Fleischmann, M.; Weckbecker, D.; Sharma, S.; Pankratov, O.; Shallcross, S. Electron-Phonon Scattering and in-Plane Electric Conductivity in Twisted Bilayer Graphene. *Phys. Rev. B* **2016**, 94 (24), No. 245403.
- (52) Das Sarma, S.; Wu, F. Electron-Phonon and Electron-Electron Interaction Effects in Twisted Bilayer Graphene. *Annals of Physics* **2020**, *417*, No. 168193.
- (53) Wang, H.; Hu, S.; Takahashi, K.; Zhang, X.; Takamatsu, H.; Chen, J. Experimental Study of Thermal Rectification in Suspended Monolayer Graphene. *Nat. Commun.* **2017**, *8* (1), 15843.
- (54) Zhang, Y.; Lv, Q.; Wang, H.; Zhao, S.; Xiong, Q.; Lv, R.; Zhang, X. Simultaneous Electrical and Thermal Rectification in a Monolayer Lateral Heterojunction. *Science* **2022**, *378* (6616), 169–175
- (55) Frisenda, R.; Molina-Mendoza, A. J.; Mueller, T.; Castellanos-Gomez, A.; Van Der Zant, H. S. J. Atomically Thin p-n Junctions Based on Two-Dimensional Materials. *Chem. Soc. Rev.* **2018**, 47 (9), 3339–3358.
- (56) Plimpton, S. Fast Parallel Algorithms for Short-Range Molecular Dynamics. *J. Comput. Phys.* **1995**, *117* (1), 1–19.
- (57) Jiang, J.-W. Misfit Strain-Induced Buckling for Transition-Metal Dichalcogenide Lateral Heterostructures: A Molecular Dynamics Study. *Acta Mech. Solida Sin.* **2019**, 32 (1), 17–28.
- (58) Rappe, A. K.; Casewit, C. J.; Colwell, K. S.; Goddard, W. A.; Skiff, W. M. UFF, a Full Periodic Table Force Field for Molecular Mechanics and Molecular Dynamics Simulations. *J. Am. Chem. Soc.* 1992, 114 (25), 10024–10035.
- (59) Jiang, J.-W.; Park, H. S.; Rabczuk, T. Molecular Dynamics Simulations of Single-Layer Molybdenum Disulphide (MoS₂):

- Stillinger-Weber Parametrization, Mechanical Properties, and Thermal Conductivity. J. Appl. Phys. 2013, 114 (6), No. 064307.
- (60) Sääskilahti, K.; Oksanen, J.; Tulkki, J.; Volz, S. Role of Anharmonic Phonon Scattering in the Spectrally Decomposed Thermal Conductance at Planar Interfaces. *Phys. Rev. B* **2014**, 90 (13), No. 134312.
- (61) Sääskilahti, K.; Oksanen, J.; Volz, S.; Tulkki, J. Frequency-Dependent Phonon Mean Free Path in Carbon Nanotubes from Nonequilibrium Molecular Dynamics. *Phys. Rev. B* **2015**, *91* (11), No. 115426.
- (62) Fan, Z.; Pereira, L. F. C.; Wang, H.-Q.; Zheng, J.-C.; Donadio, D.; Harju, A. Force and Heat Current Formulas for Many-Body Potentials in Molecular Dynamics Simulations with Applications to Thermal Conductivity Calculations. *Phys. Rev. B* **2015**, *92* (9), No. 094301.
- (63) Soler, J. M.; Artacho, E.; Gale, J. D.; García, A.; Junquera, J.; Ordejón, P.; Sánchez-Portal, D. The SIESTA Method for Ab Initio Order- N Materials Simulation. *J. Phys.: Condens. Matter* **2002**, *14* (11), 2745–2779.
- (64) Büttiker, M.; Imry, Y.; Landauer, R.; Pinhas, S. Generalized Many-Channel Conductance Formula with Application to Small Rings. *Phys. Rev. B* **1985**, *31* (10), 6207–6215.
- (65) Brandbyge, M.; Mozos, J.-L.; Ordejón, P.; Taylor, J.; Stokbro, K. Density-Functional Method for Nonequilibrium Electron Transport. *Phys. Rev. B* **2002**, *65* (16), No. 165401.
- (66) Kienle, D.; Cerda, J. I.; Ghosh, A. W. Extended Hückel Theory for Band Structure, Chemistry, and Transport. I. Carbon Nanotubes. *J. Appl. Phys.* **2006**, *100* (4), No. 043714.
- (67) Wasfi, A.; Awwad, F. Semi-Empirical Modeling for DNA Bases via Z-Shaped Graphene Nanoribbon with a Nanopore. In 2019 IEEE 13th International Conference on Nano/Molecular Medicine & Engineering (NANOMED); IEEE: Gwangju, Korea (South), 2019; pp 16–21.
- (68) Dick, D.; Fuchs, F.; Schuster, J.; Gemming, S. An Extended Hückel Theory Parameter Set for Efficient Electronic Structure Calculations of SiGe Alloys. *Phys. Status Solidi RRL* **2025**, No. 2500087.
- (69) Stokbro, K.; et al. Semiempirical Model for Nanoscale Device Simulations. *Phys. Rev. B* **2010**, 82 (7), No. 075420.
- (70) Levchenko, S. V.; Ren, X.; Wieferink, J.; Johanni, R.; Rinke, P.; Blum, V.; Scheffler, M. Hybrid Functionals for Large Periodic Systems in an All-Electron, Numeric Atom-Centered Basis Framework. *Comput. Phys. Commun.* **2015**, 192, 60–69.
- (71) Heyd, J.; Scuseria, G. E.; Ernzerhof, M. Hybrid Functionals Based on a Screened Coulomb Potential. *J. Chem. Phys.* **2003**, *118* (18), 8207–8215.
- (72) Heyd, J.; Peralta, J. E.; Scuseria, G. E.; Martin, R. L. Energy Band Gaps and Lattice Parameters Evaluated with the Heyd-Scuseria-Ernzerhof Screened Hybrid Functional. *J. Chem. Phys.* **2005**, *123* (17), 174101.
- (73) Heyd, J.; Scuseria, G. E. Efficient Hybrid Density Functional Calculations in Solids: Assessment of the Heyd–Scuseria–Ernzerhof Screened Coulomb Hybrid Functional. *J. Chem. Phys.* **2004**, *121* (3), 1187–1192.
- (74) Grimme, S. Semiempirical GGA-type Density Functional Constructed with a Long-range Dispersion Correction. *J. Comput. Chem.* **2006**, 27 (15), 1787–1799.



CAS BIOFINDER DISCOVERY PLATFORM™

CAS BIOFINDER HELPS YOU FIND YOUR NEXT BREAKTHROUGH FASTER

Navigate pathways, targets, and diseases with precision

Explore CAS BioFinder

